Acta Pharmaceutica Sinica B 2024;14(2):821−835

Chinese Pharmaceutical Association
Institute of Materia Medica, Chinese Academy of Medical Sciences

Acta Pharmaceutica Sinica B

www.elsevier.com/locate/apsb
www.sciencedirect.com

ORIGINAL ARTICLE

Self-sufficient nanoparticles with dual-enzyme activity trigger radical storms and activate cascade-amplified antitumor immunologic responses

Liping Bai[†], Jin Yang[†], Siting Yu, Zhongzheng Xiang, Yuanyuan Zeng, Meiling Shen, Xiaorong Kou, Qinjie Wu[*], Changyang Gong[*]

Department of Biotherapy, Cancer Center and State Key Laboratory of Biotherapy, West China Hospital, Sichuan University, Chengdu 610041, China

Received 9 May 2023; received in revised form 21 July 2023; accepted 8 August 2023

KEY WORDS

Dual-enzyme activity;
Radiotherapy;
Chemodynamic therapy;
Fenton-like reaction;
Radical storms;
Immunogenic cell death;
Tumor microenvironment;
Systemic immunity

Abstract Radiotherapy (RT) can potentially induce systemic immune responses by initiating immunogenic cell death (ICD) of tumor cells. However, RT-induced antitumor immunologic responses are sporadic and insufficient against cancer metastases. Herein, we construct multifunctional self-sufficient nanoparticles (MARS) with dual-enzyme activity (GOx and peroxidase-like) to trigger radical storms and activate the cascade-amplified systemic immune responses to suppress both local tumors and metastatic relapse. In addition to limiting the Warburg effect to actualize starvation therapy, MARS catalyzes glucose to produce hydrogen peroxide (H_2O_2), which is then used in the Cu^+-mediated Fenton-like reaction and RT sensitization. RT and chemodynamic therapy produce reactive oxygen species in the form of radical storms, which have a robust ICD impact on mobilizing the immune system. Thus, when MARS is combined with RT, potent systemic antitumor immunity can be generated by activating antigen-presenting cells, promoting dendritic cells maturation, increasing the infiltration of cytotoxic T lymphocytes, and reprogramming the immunosuppressive tumor microenvironment. Furthermore, the synergistic therapy of RT and MARS effectively suppresses local tumor growth, increases mouse longevity, and results in a 90% reduction in lung metastasis and postoperative recurrence. Overall, we provide a viable approach to treating cancer by inducing radical storms and activating cascade-amplified systemic immunity.

*Corresponding authors.
E-mail addresses: cellwqj@163.com (Qinjie Wu), chygong14@163.com (Changyang Gong).
[†]These authors made equal contributions to this work.
Peer review under the responsibility of Chinese Pharmaceutical Association and Institute of Materia Medica, Chinese Academy of Medical Sciences.

https://doi.org/10.1016/j.apsb.2023.10.003

1. Introduction

As one of the most mainstream cancer treatment strategies, radiotherapy (RT) has been applied to over half of the tumor patients for therapeutic and palliative purposes in clinical practice[1]. During radiotherapy, high-energy ionizing radiation (*e.g.*, X-ray, γ-ray, etc.) and particle radiation (*e.g.*, electrons, neutrons, protons, etc.) directly or indirectly generate DNA damage to induce tumoricidal effects[2,3]. The reactive oxygen species (ROS) generated by RT can induce immunogenic cell death (ICD)[4]. The tumor-associated antigens (TAAs) released by tumor cells undergoing ICD are internalized and processed by antigen-presenting cells (APCs) and presented to T cells[5]. Meanwhile, the ICD-associated damage-associated molecular patterns (DAMPs) as adjuvant analogs that stimulate dendritic cells (DCs) maturation, cytotoxic T lymphocytes activation, and the secretion of various cytokines, thereby initiating systemic immunity and leading to tumor regression in non-irradiated patients (called the abscopal effect)[4,6–8]. However, the RT-mediated abscopal effect is unpredictable and insufficient against metastatic tumors due to factors such as inefficient induction of ICD and immunosuppressive tumor microenvironment[9–12]. Therefore, multiple approaches to amplify RT-mediated systemic immune responses and extend the application of RT remain an essential focus in the field of cancer therapy.

Various ROS-mediated cancer treatment strategies have been developed for tumor therapy, including chemotherapy, photodynamic therapy (PDT) and sonodynamic therapy (SDT), etc[13–16]. However, their therapy efficacies are severely constrained by drawbacks, such as multidrug resistance, hypoxic tumor microenvironment, shallow field penetration, and high equipment cost. As a promising treatment modality, chemodynamic therapy (CDT) can utilize endogenous excessive production of hydrogen peroxide (H_2O_2) to generate more toxic hydroxyl radicals (•OH) *via* metal ions (*e.g.*, Cu^+, Fe^{2+}, Mn^{2+}, Mo^{4+}, Ti^{3+}, etc.)-mediated Fenton/Fenton-like reaction in a mild acidic medium[17–20]. Intratumoral H_2O_2 (∼100 μmol/L) is significantly higher than that in normal tissues but not enough to sustainably generate •OH. The glucose oxidase (GOx) can catalyze glucose oxidation to generate H_2O_2 and gluconic acid, which disrupts glucose's essential function in tumor cell proliferation and metabolism[18,19,21,22]. Notably, this procedure not only generates H_2O_2 for CDT, but also limits the Warburg effect of tumor cells, which facilitates starvation therapy and dampens the suppressive function of regulatory T cells (Tregs)[23]. Therefore, ROS generated by CDT can enhance RT-mediated ICD to activate robust systemic immune responses that can inhibit tumor metastasis.

Toll-like receptors (TLRs)-mediated modulation of the tumor microenvironment is another intriguing strategy for further boosting RT-induced antitumor immunity[24–26]. TLRs, expressed mainly by DCs, B cells, natural killer cells, and macrophages, can recognize ICD-associated DAMPs to trigger the antitumor immune responses[27]. Resiquimod (R848) is a small-molecule TLR7/8 receptor agonist that, upon binding to TLR7/8, releases multiple immunomodulatory cytokines and triggers a cascade of signaling pathways, all of which improve antigen processing and presenting ability of APCs and polarize T-cell responses[25,28,29]. It has been reported that compared with RT alone, the RT combined with R848 significantly facilitates DCs maturation and the $CD8^+$ T lymphocyte infiltration, effectively inhibits tumor growth, and prolongs the survival time of tumor-bearing mice[30–32]. However, the hydrophobicity of R848 severely restricts its applicability as its bioavailability is poor when administered systemically. Because of its high biocompatibility and physiological stability, human serum albumin (HSA) makes a tremendous therapeutic carrier for addressing the hydrophobicity of R848[33–35]. Thus, R848 is crucial for amplifying RT-mediated systemic immune responses against metastatic relapse by activating the tumor immune microenvironment.

Herein, we designed multifunctional self-sufficient nanoparticles (MARS) with dual-enzyme activity to initiate radical storms and generate the cascade-amplified systemic immune responses for inhibiting tumor growth, metastasis, and postoperative recurrence (Fig. 1). MARS was constructed *via* the albumin-mediated biomineralization-like method, containing GOx natural enzyme, Cu^+ peroxidase-like nanozyme, and R848 agonist. When reaching the tumor site, MARS oxidized glucose to gluconic acid and H_2O_2, which not only restricted the Warburg effect of tumor cells to achieve starvation therapy and reduced the inhibitory effect of Tregs, but also achieved H_2O_2 self-supplying to generate •OH *via* Cu^+-mediated Fenton-like reaction. Meanwhile, ionizing radiation could transform H_2O_2 into more noxious ROS, which boosted RT-mediated tumoricidal effects in tumor location[36]. Then, radical storms formed from ROS generated by RT and CDT could induce a robust ICD effect to initiate systemic immune responses. The combination with RT, the MARS facilitated the maturation and migration of DCs, promoted the tumor-infiltrating T cells, and reversed the immunosuppressive tumor microenvironment to stimulate the potent systemic antitumor immune responses. Overall, the collaborative treatment of RT and MARS was able to drastically inhibit tumor growth, prolong mice's survival time, and prevent the recurrence and metastasis of triple-negative breast cancer (TNBC). Therefore, our therapeutic approach can be a promising strategy to trigger radical storms and cascade-amplified RT-mediated systemic antitumor immune responses.

2. Materials and methods

2.1. Materials and reagents

Copper (II) chloride dihydrate ($CuCl_2 \cdot 2H_2O$), tannic acid (TA), sodium hydroxide (NaOH), and acetone were supplied from Aladdin Reagent Co., Ltd. (Shanghai, China). HSA was purchased from CSL Behring (Marburg, Germany). R848 and 3,3′,5,5′-tetramethylbenzidine (TMB) were provided by Macklin Biochemical Co., Ltd. (Shanghai, China). Soybean oil, 2′,7′-dichlorodihydrofluorescein diacetate (H_2DCFDA), [3-(4,5-dimethylthiazol-2-yl)-2,5-diphenyl] tetrazolium bromide (MTT) and GOx from

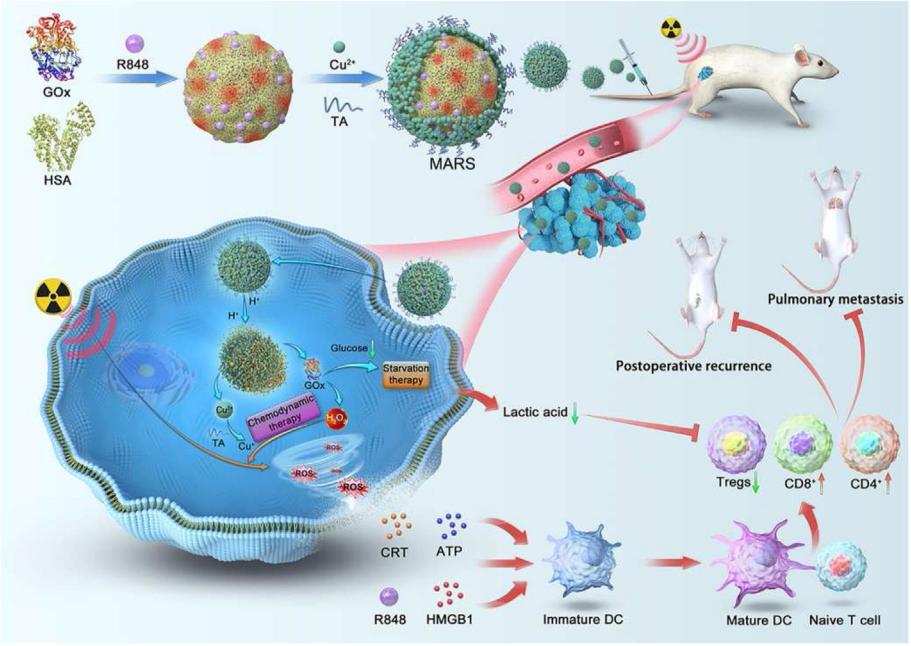

Figure 1 The synergistic therapy of radiotherapy with multifunctional self-sufficient nanoparticles (MARS) containing the dual-enzyme catalytic activity initiated radical storms and activated the cascade-amplified systemic immune responses against the local tumors, postoperative recurrence, and pulmonary metastases.

Aspergillus niger were purchased from Sigma−Aldrich Chemical Co., Ltd. (MO, USA). All chemical reagents were of analytical quality and were utilized without purification. Adenosine triphosphate (ATP) assay kit, 4,6-diamidino-2-phenylindole (DAPI), H_2O_2 assay kit, and glucose assay kit were obtained from Beyotime Biotechnology Co., Ltd. (Shanghai, China). Annexin V-fluorescein isothiocyanate (FITC)/propidium iodide (PI) cell apoptosis kit was acquired from 4A Biotech. Co., Ltd. (Beijing, China). All flow cytometry antibodies were purchased from Biolegend (San Diego, CA, USA) or Bioss Co., Ltd. (Beijing, China) (Supporting Information Table S1). The enzyme-linked immunosorbent assay (ELISA) kits for cytokines were obtained from Biolegend (San Diego, CA, USA).

2.2. *Preparation of MARS*

First, HSA (40 mg) and GOx (0.2 mg) were dissolved in 4 mL of deionized water and sonicated for 3 min using an ultrasonic probe (Ningbo Xinyi Ultrasonic Equipment Co., Ltd., JY92-IIN, China) with a power of 130 W. Then 100 μL of acetone containing R848 and 40 μL of soybean oil were added into the reaction system, and it was sonicated for 6 min using an ultrasonic probe with a power of 455 W. The obtained mixture was concentrated to remove acetone. Finally, $CuCl_2 \cdot 2H_2O$ (1.7 mg) and TA (2 mg) were introduced, and the resultant suspension was stirred overnight to obtain MARS. The product was concentrated by ultrafiltration (Sigma−Aldrich Chemical Co., Ltd., 30 kDa MWCO, MO, USA) and washed multiple times with deionized water. The HAS-TA-Cu^{2+} (HTC) was prepared without GOx and R848, while all other conditions remained unchanged.

2.3. *Characterization and instruments*

The size and surface zeta potential of nanoparticles were characterized by dynamic light scattering measurement (Malvern, Zeta-sizer NanoZS90, UK). Fourier transform infrared spectrometer (FT-IR) measurements were taken between 4000 and 500 cm^{-1} (Thermo Nicolet Corporation, Nicolet 6700, USA). The transmission electron microscope (TEM, Hitachi, HT7800, Japan) was used to observe the morphology of nanoparticles. The R848 concentration in MARS was measured by UV−Vis spectrophotometer (SHIMADZU, UV-2600, Japan). The Cu ions content was measured by the inductively coupled plasma optical emission spectrometer (ICP-OES, PerkinElmer, Avio 220 Max, USA). The element mapping of MARS was analyzed by TEM-EDS (JEOL, JEM2200FS, Japan).

2.4. *Cell culture and animals*

This study used murine mammary carcinoma (4T1) cells obtained from American Type Culture Collection (ATCC, USA) as a model cell. 4T1 cells were cultured in Roswell Park Memorial Institute (RPMI) 1640 medium (Gibco Invitrogen, USA) supplemented with 10% fetal bovine serum (FBS), 1% penicillin, and 1% streptomycin at 37 °C in an atmosphere containing 5% CO_2.

Female BALB/c mice (6−8 weeks) were acquired from HUAFUKANG Bioscience Co., Ltd. (Beijing, China). All animal experiments were conducted following the guidelines established by Sichuan University's Institutional Animal Care and Treatment Committee (Chengdu, China).

2.5. *pH-Responsive degradation of MARS in vitro*

Dialysis bags containing MARS (1 mL, 45 mg/mL) were placed into plastic tubes containing 9 mL of phosphate-buffered saline (PBS, pH = 7.4, 6.5, or 5.5) to investigate the effect of pH on MARS degradation. Then, the tubes were shaken at 37 °C under 100 rpm (ZHICHENG, ZHWY-211D, China). At given intervals, 9 mL of media was removed from the solution outside the bags and replaced with fresh PBS with the same volume and pH.

Preliminary to the analysis, the sample must be nitrated with aqua regia. A UV−Vis spectrophotometer (SHIMADZU) and an ICP-OES (PerkinElmer) were used to measure the amounts of R848 and Cu ions in the collected solutions, respectively.

2.6. Catalytic ability of MARS

MARS was added to the tubes and mixed with different amounts of glucose solutions (0, 1, 5, or 10 mmol/L) at room temperature to evaluate the catalytic capacity of MARS. The reaction solutions were collected to detect H_2O_2 concentrations by an H_2O_2 assay kit and pH values by a pH meter (F3-Standard, Mettler Toledo, China) at different time points, respectively. The glucose consumption-ability of MARS was measured with a glucose assay kit.

2.7. Chemodynamic activity of MARS

MARS (360 μL, 45 mg/mL), TMB (20 μL, 50 mmol/L), and various amounts of glucose in PBS (pH = 5.5) were mixed within the tubes. The system had a 400 μL total volume. Then the solution was agitated at 37 °C in dark conditions for 10 h. The respective concentrations of glucose in the final reaction system were 0, 0.25, 0.625, 1.25, 2.5, and 5 mmol/L, respectively. The generation of hydroxyl radical (•OH) was determined by measuring the absorbance of the resulting suspension in the range of 500−800 nm. MARS-treated TMB solution was used as a control without glucose.

2.8. Cell viability assessment

For *in vitro* cytotoxicity evaluations, 4T1 cells were inoculated in 96-well plates at a density of 4×10^3 cells per well and cultured at 37 °C for 12 h. The cell culture medium was substituted with a fresh medium containing different R848, HTC, or MARS concentrations, followed by an additional 24 h incubation. The relative cell viability was measured by utilizing the standard MTT assay method. Each plate received 5 mg/mL of MTT solution and was incubated for 3 h. They were measured the absorbance at 570 nm, allowing for cell viability assessment. The control group was established as the cells without receiving pharmacological treatment.

4T1 cells (4×10^3 cells per well) were seeded in 96-well plates and incubated for 12 h to determine the glucose-dependent cytotoxicity of MARS. After that, we replaced the original media with a fresh RPMI 1640 medium containing various concentrations of MARS and glucose (0, 1, 5, or 10 mmol/L). The MTT assay was performed after 24 h to determine the relative cell viability.

For the clonogenic assay, 4T1 cells were inoculated at a density of 1×10^3 cells/well in 6-well plates for 12 h. Then, the cells were treated with PBS, HTC, or MARS. After 4 h of incubation, the cells were exposed to 4 Gy of X-rays. These cells were cultured at 37 °C with 5% CO_2 in a humidified atmosphere. When evident cell colonies formed in the PBS group, the cell culture was discontinued. The cells were fixed in 4% paraformaldehyde for 10 min, rinsed with cold PBS, stained with 0.1% crystal violet for 5 min, and rinsed with cold PBS once macroscopic cell colonies formed. Cell colonies with more than 50 cells were counted.

The Annexin V-FITC/PI cell apoptosis reagent was used to examine the effect of MARS+RT on cellular apoptosis/necrosis. Briefly, 4T1 cells (5×10^4 cells per well) were seeded and incubated overnight in 12-well plates. Then, each well was refilled with fresh culture medium containing PBS, HTC, or MARS for 4 h incubation. Then the cells were irradiated with X-rays at 4 Gy. After another 20 h of incubation, the cells were collected, rinsed with cold PBS, sequentially stained with Annexin V and PI, and then analyzed using the flow cytometer (Agilent, NovoCyte, USA).

2.9. ROS detection

To investigate the production of ROS following MARS+RT treatment, 1×10^5 4T1 cells per well were added to 12-well plates. After overnight attachment, cells received treatment with saline, HTC, or MARS for 4 h. After that, the cells were exposed to 4 Gy of radiation. The cell culture medium was removed and washed with PBS. H_2DCFDA (10 μmol/L) was introduced and incubated in the dark at 37 °C for 20 min. Then, the cells were rinsed 3 times with cold PBS. At last, the expression of ROS was investigated by flow cytometry (Agilent) and confocal microscopy (Olympus, IX73, Japan).

2.10. In vitro ICD assessment

Briefly, 2×10^5 4T1 cells were inoculated into per confocal dish (Φ = 15 mm) and cultured for 12 h. The cells were then treated for 24 h with PBS, HTC, MARS, RT, HTC+RT, or MARS+RT. Next, the cells were washed 3 times with PBS, fixed with 4% paraformaldehyde, and blocked for 30 min at room temperature. Then the cells were incubated overnight at 4 °C with rabbit anti-mouse CRT antibody (Abcam, Cambridge, UK). After rinsing with PBS, the Alexa Fluro 488 conjugated goat anti-rabbit IgG H&L (Abcam, Cambridge, UK) was used to stain the cells for 1 h at 25 °C. Then cells were washed and stained with DAPI. The difference between rabbit anti-mouse high mobility group box 1 (HMGB1) antibody (Abcam, Cambridge, UK) and anti-CRT staining was that cells were incubated with 0.1% Triton X-100 at 25 °C for 10 min. The confocal laser scanning microscope (CLSM, ZEISS, LSM880, Germany) was used to acquire the images of all groups. Additionally, flow cytometry (Agilent) was also utilized to measure the expression of CRT and HMGB1. After different treatments, an ATP detection reagent measured the concentration of ATP in the medium.

2.11. DNA damages

5×10^5 4T1 cells per dish were seeded in confocal dishes (Φ = 15 mm) and incubated at 37 °C for 12 h. After 4 h of incubation with PBS, HTC, or MARS, the cells were subjected to 4 Gy of X-ray radiation and incubated for another 1 h. The cells were fixed with 4% paraformaldehyde for 10 min, permeabilized with 0.2% Triton X-100 for 10 min, blocked for 30 min at room temperature, and stained overnight at 4 °C with rabbit anti-mouse γ-$H_2A\chi$ antibody (Bioss, Beijing, China). After that, the cells were stained for 1 h at 25 °C with Alexa Fluor 555 conjugated goat anti-rabbit IgG H&L (Abcam, Cambridge, UK) and DAPI. Eventually, these cells were imaged with CLSM (ZEISS).

2.12. Bone marrow-derived dendritic cells (BMDCs) maturation in vitro

The bone marrow cells were collected from the hind extremities of 6- to 8-week-old C57BL/6 mice. Next, a red blood cell lysis buffer was added to lyse the red blood cells. The obtained cells were rinsed with serum-free RPMI 1640 supplemented and then cultured in RPMI 1640 medium containing 10% inactivated FBS, GM-CSF (20 ng/mL), rMuIL-4 (10 ng/mL), and

β-mercaptoethanol (50 nmol/L). The cultivated medium was replaced every 2 days. On the 6th day, BMDCs were extracted and co-cultured for 24 h with 4T1 cells subjected to various treatments. Finally, the obtained cells were stained with maturation-related markers (anti-mouse CD86 and anti-mouse CD80) on BMDCs and analyzed by flow cytometry (Agilent).

2.13. Antitumor effectiveness in vivo

The antitumor efficacy of MARS with RT was evaluated on female BALB/c mice in a subcutaneous tumor model of TNBC. Firstly, subcutaneous injections of 4T1 cells (100 μL, 1×10^6 cells) were made into the right flanks of the mice. The mice with tumor volumes ~80 mm^3 were randomized into 6 groups and given intravenous injections of saline, HTC, or MARS (HTC: 112.5 mg/kg, GOx: 470 μg/kg, R848: 2 mg/kg) every 2 days for 4 times, respectively. After 4 h following the second i.v. injection of saline, HTC, or MARS, the mice were irradiated with X-rays at 4 Gy. Each mouse's tumor volume and weight were tracked every other day. Tumor volumes were determined using the following Eq. (1):

$$\text{Volume } (mm^3) = \text{Length} \times \text{Width}^2 \times 0.5 \quad (1)$$

On Day 15, all mice were sacrificed, and their tumor tissues were collected, photographed, and weighed immediately. In addition, the tumor tissues were subjected to hematoxylin-eosin (H&E) staining, terminal deoxynucleotidyl transferase-mediated deoxyuridine triphosphate nick-end labeling (TUNEL) staining, and immunohistochemistry (IHC) to further evaluate the antitumor effect. The collected primary organs (heart, liver, spleen, lung, and kidney) were analyzed for system toxicity by H&E staining. In addition, the survival time profiles of mice with tumors following therapy were monitored until the conclusion of the experiment.

2.14. In vivo antitumor immunity assessment

Mice with 4T1 tumors were randomly split into 6 treatment groups ($n = 3$): saline, HTC, MARS, RT, HTC+RT, or MARS+RT. RT was administered 4 h after the second intravenous injection at a dose of 4 Gy. After completing the entire treatment, we euthanized them and harvested their tumors, spleens, and tumor-draining lymph nodes (TDLNs) to make a single-cell suspension. The cell suspension was stained with anti-mouse CD11c, anti-mouse CD86, and anti-mouse CD80 antibodies for flow cytometry (Agilent) to investigate DCs at different maturation levels. The tumor single-cell suspensions were labeled with fluorophore-conjugated antibodies (anti-mouse CD3, anti-mouse CD4, anti-mouse CD25, and anti-mouse FoxP3) and evaluated by flow cytometry (Agilent) to identify Tregs. The TDLNs cell suspensions were stained with anti-mouse CD3, anti-mouse CD8a, and anti-mouse CD4 antibodies and then identified using flow cytometry (Agilent) to assess T-cell activation. The cytokine levels of interferon-gamma (IFN-γ) and tumor necrosis factor-α (TNF-α) in the serum were analyzed using corresponding ELISA kits according to the reagent instructions.

2.15. In vivo lung metastasis and postoperative recurrence inhibitory effects

Orthotopically injected luciferase-labeled 4T1 (Luc-4T1) cells were used to imitate primary tumors in female BALB/c mice's fourth mammary fat pad. The recurrence model was built using data from surgeries performed on 90% of primary tumors while their tumor volumes reached ~100 mm^3. Then, mice were intravenously injected with 4T1 cells (1×10^6 cells per mouse) before treatments to develop the pulmonary metastatic model and randomly separated into four groups ($n = 5$): saline, MARS, RT, and MARS+RT. D-luciferin (150 mg/kg) was given intraperitoneally to the mice on Days 6, 12, and 18 after the treatments began, and the bioluminescence was imaged using the IVIS imaging system (PerkinElmer). After being monitored for 18 days, we euthanized the mice and collected, weighed, and photographed their tumors and lungs. For histological analysis, the lungs were paraformaldehyde-fixed and H&E-stained.

2.16. Statistical analysis

The statistical analysis was conducted using GraphPad Prism 5.0 software. The results were expressed as mean values ± standard deviation (SD), and the differences were analyzed using one-way ANOVA and two-way ANOVA. The level of significance was set at probabilities of $^*P < 0.05$, $^{**}P < 0.01$, and $^{***}P < 0.001$.

3. Results and discussion

3.1. Synthesis and characterization of MARS

MARS was prepared based on the procedures described in Fig. 2A. The solutions of HSA and GOx were mixed, added with R848 solution and soybean oil, and sonicated to produce the oil-in-water (O/W) emulsion. This method reduces the quantity of organic reagent required for R848 hydrophobicity. Then, Cu^{2+} was added to facilitate the biomineralization-like reaction. Next, TA was added to the above mixture to form stable nanoparticles by reacting with protein and Cu^{2+}. The average hydrodynamic diameter of MARS was approximately 165 nm, and it was negatively charged with a potential of −39.3 mV, as determined by dynamic light scattering (Fig. 2B and Supporting Information Fig. S1). The MARS polydispersity index (PDI) for the nanoparticles was 0.178, indicating that they dispersed well in aqueous water. In addition, MARS was stable in deionized water and PBS at 4 °C for at least 7 days (Fig. 2C and Supporting Information Fig. S2). Images captured with a TEM revealed that the MARS had a regular spherical shape (Supporting Information Fig. S3). Cu, O, C, N, and S elements were uniformly distributed in MARS, as determined by the TEM elemental mapping (Fig. 2D and F). The FT-IR spectra of MARS revealed characteristic peaks of TA (1182 and 1090 cm^{-1}, −OH vibration) and HSA (1647 and 1537 cm^{-1}, −CO−NH− vibration), confirming the formation of organic-inorganic composites (Fig. 2E)[37,38]. The minor shift in characteristic peaks in MARS indicates that Cu^{2+} coordinated with TA and interacted with the amide of HSA.

According to the UV−Vis spectrophotometer and ICP-OES measurements, the encapsulation rates of R848 and Cu were ~85.6% and ~97.3%, respectively. Due to the protonation of hydroxyl groups of TA, the coordination between Cu^{2+} and TA was destabilization when exposed to an acidic environment. As observed by TEM images, the acidic conditions (pH = 5.5) could trigger the degradation of MARS (Fig. 2G and Supporting Information Fig. S4). Moreover, the acidic-responsive degradation performance of MARS was evaluated by monitoring the concentration of Cu ions and R848 in PBS at 37 °C with varying pH

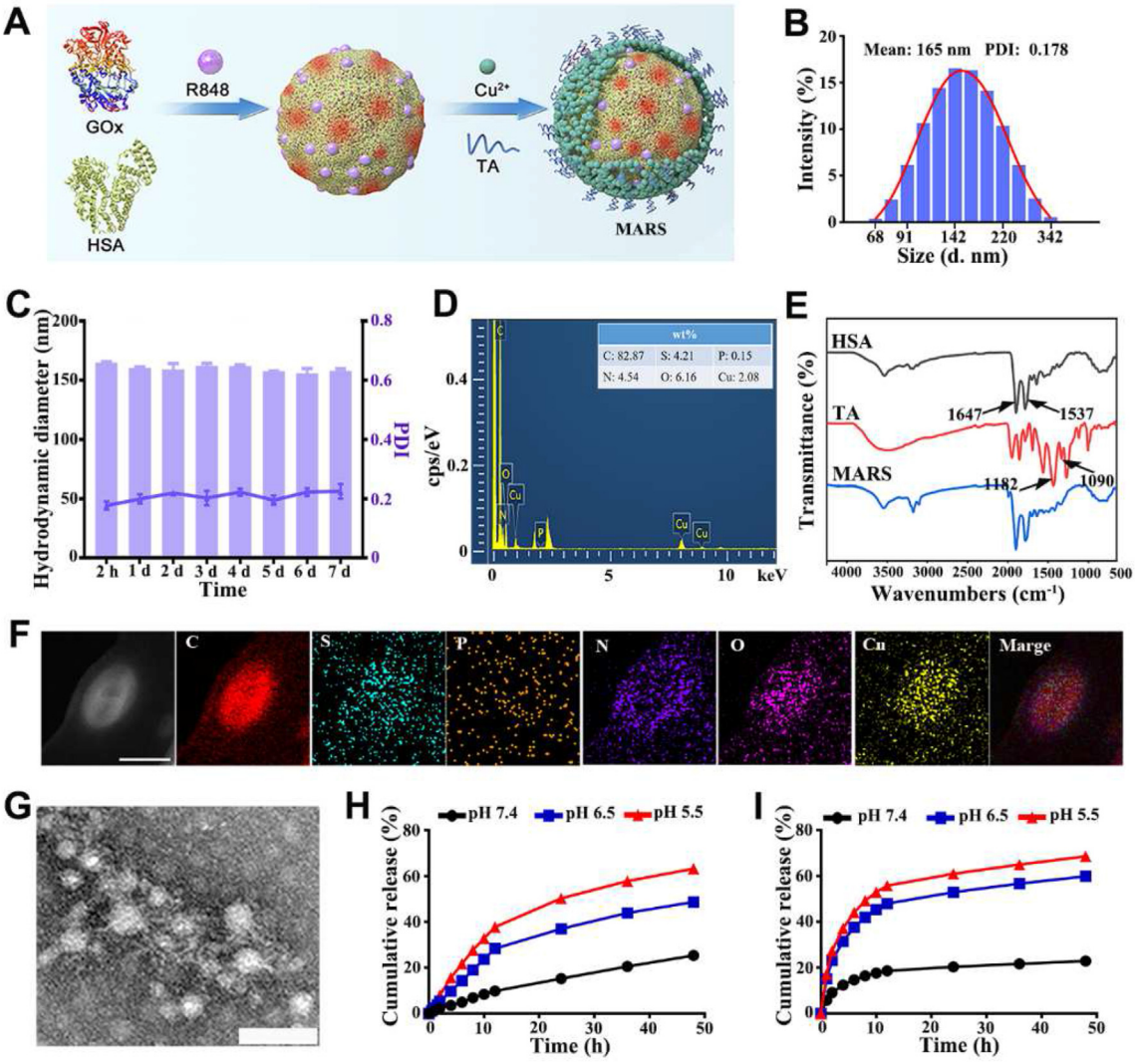

Figure 2 Preparation and characterization of MARS. (A) The MARS fabrication procedure. (B) Hydrodynamic size distribution of MARS. (C) The average diameter and polydispersity index of MARS in aqueous solution ($n = 3$). (D) Energy dispersive spectrometer of MARS. (E) FT−IR spectra of HSA, TA, and MARS. (F) The representative TEM elemental mapping of MARS. Scale bar = 250 nm. (G) The representative TEM images of MARS in PBS (pH = 5.5). Scale bar = 100 nm. The release profile of Cu ions (H) and R848 (I) in PBS with various pH.

values. As anticipated, the release of Cu ions increased ∼1.3- and ∼2.5-fold at pH 6.5 and 5.5, respectively, relative to that at pH 7.4 (Fig. 2H). Within 48 h, the amount of R848 released at pH 5.5 (∼68.5%) was considerably more significant than those at pH 7.4 (∼22.8%) and 6.5 (∼59.8%) (Fig. 2I and Supporting Information Fig. S5). The drug release profiles of MARS were sustained and acid-responsive. Therefore, it was foreseeable that MARS could be a multifunctional nanocarrier capable of delivering antitumor medications to the tumor region *via* its acidic responsiveness.

3.2. *The evaluation of MARS double enzymatic activity*

According to numerous reports, GOx could facilitate glucose consumption to generate H_2O_2 and gluconic acid. In addition, MARS with peroxidase-like catalytic activity was able to convert H_2O_2 to produce •OH *via* a Cu^+-mediated Fenton-like reaction (Fig. 3A). Therefore, we verified the H_2O_2 self-sufficient cascade catalytic performance of the MARS. First, the catalytic capability of MARS was determined by measuring the glucose consumption, H_2O_2 production, and pH variation (Fig. 3B−D). The glucose concentration gradually decreased progressively over time in the MARS group, indicating that MARS consumed glucose in a time-dependent manner. Moreover, MARS increased H_2O_2 production at high glucose levels. However, owing to the absence of GOx, the glucose consumption and H_2O_2 production in the HTC group followed the same pattern as that of the control group. In the MARS group, the pH variation caused by the generated gluconic acid decreased significantly at high glucose concentrations (from 7.3 to 5.3 in 5 mmol/L glucose). Then, we further evaluated the •OH generated by MARS-mediated Fenton-like reaction. TMB was utilized to detect the production of •OH, as it could be oxidized by •OH to produce a blue-green color and maximum absorbance at 652 nm. The absorbance of TMB increased considerably as glucose concentration increased (Fig. 3E and Supporting Information Fig. S6). These results demonstrated that MARS could generate •OH by Cu^+-mediated Fenton-like reaction in PBS (pH = 5.5) containing glucose.

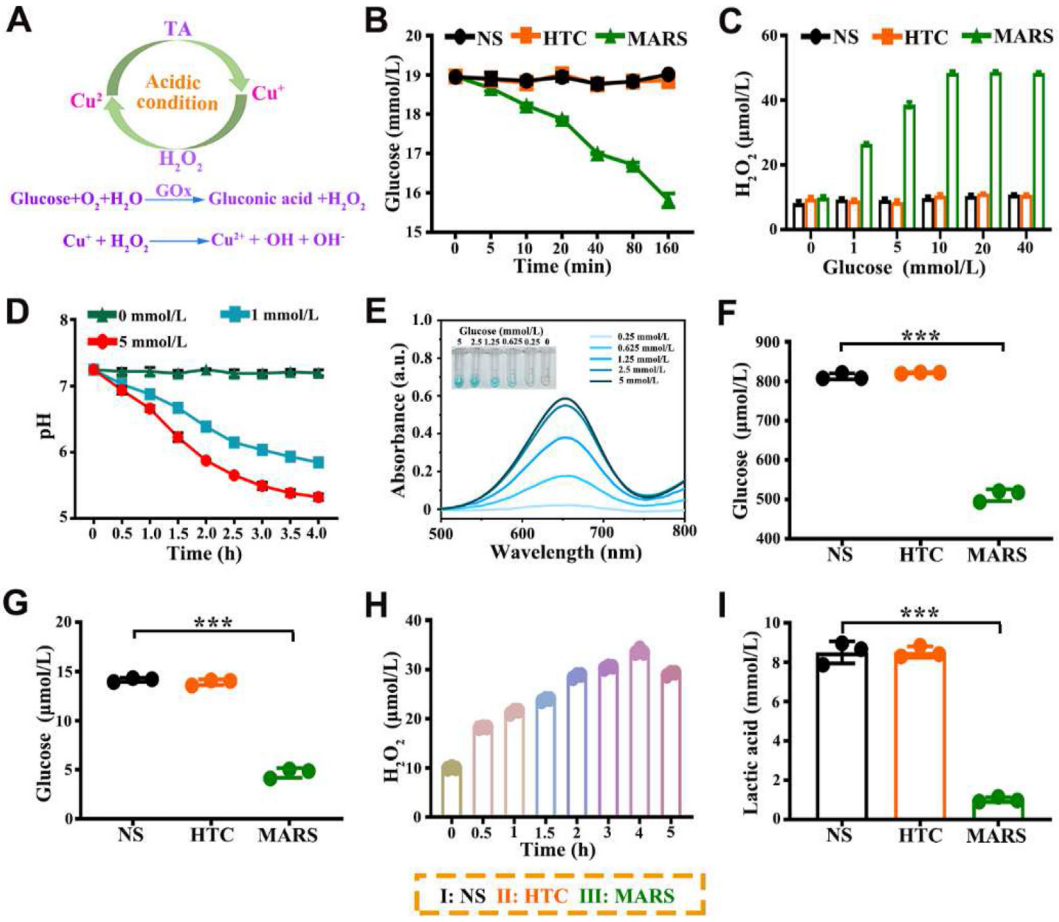

Figure 3 The cascade catalytic reaction by MARS. (A) Schematic illustration of H_2O_2 self-supplying by MARS. (B) Glucose consumption in NS, HTC, and MARS groups. (C) The concentration of H_2O_2 generated in PBS with various glucose concentrations. (D) pH decrease arising from generating lactic acid by the reaction between MARS and different glucose concentrations. (E) Absorbance spectrum and photograph (inset) of TMB solution treated with MARS and various glucose concentrations (PBS, pH = 5.5). The glucose levels in the medium (F) and 4T1 cells (G) in NS, HTC, and MARS groups. (H) The intracellular H_2O_2 levels after being treated with MARS at different times. (I) The lactic acid concentrations in the medium after various treatments. Data are presented as mean ± SD ($n = 3$). ***$P < 0.001$.

We further confirmed the H_2O_2 self-sufficient cascade catalytic reaction of MARS in 4T1 cells. As depicted in Fig. 3F and G, MARS not only consumed glucose from the culture medium but also depleted glucose from within the cells. Therefore, MARS would play a crucial function in the tumor microenvironment and tumor cells' glucose consumption. Using an H_2O_2 assay kit, the concentration of H_2O_2 was measured in 4T1 cells subjected to MARS at various times (Fig. 3H). When 4T1 cells were treated with MARS, the H_2O_2 levels in intracellular increased significantly with prolonged incubation. However, the H_2O_2 concentration decreased after being treated for 5 h, which could be attributed to the Cu^+ catalyzing H_2O_2 decomposition at weakly acidic conditions. Moreover, MARS could diminish lactic acid production by inhibiting the Warburg effect of tumor cells. We measured the lactic acid levels in the medium following various treatments with the lactic acid assay kit. After MARS treatment, the concentration of lactic acid decreased dramatically in the culture medium (Fig. 3I). The results above suggested that MARS could initiate starvation therapy to accomplish H_2O_2 self-supplying and reduce the production of lactic acid, and trigger Cu^+-mediated Fenton-like reaction.

3.3. *In vitro cytotoxicity of MARS*

The antitumor efficacy of MARS was determined using an MTT assay on 4T1 cells. Firstly, the 4T1 cells were incubated with various amounts of R848, HTC, Cu^{2+}, and MARS in a serum-containing standard RPMI medium. As shown in Supporting Information Fig. S7, there were no significant inhibitions of proliferation in the R848, HTC, or Cu^{2+} groups at the same MARS concentration. However, MARS exhibited significant cytotoxicity with a half inhibitory concentration (IC50) value of ∼7.0 μg/mL (Fig. 4A)., The cytotoxic effects of MARS were subsequently investigated in media containing different concentrations of glucose (Fig. 4B). The results demonstrated a decrease in cell viability as glucose concentration increased, indicating that the toxicity of MARS was glucose-dependent. The uptake efficacy of MARS was determined using flow cytometry (Supporting Information Fig. S8). The MARS exhibited significant time-dependent endocytosis and attained maximum intracellular uptake efficiency after 4 h of incubation. Thus, the cells were irradiated after receiving various treatments for 4 h in subsequent cell experiments. Furthermore, the radiation dose was chosen as 4 Gy based

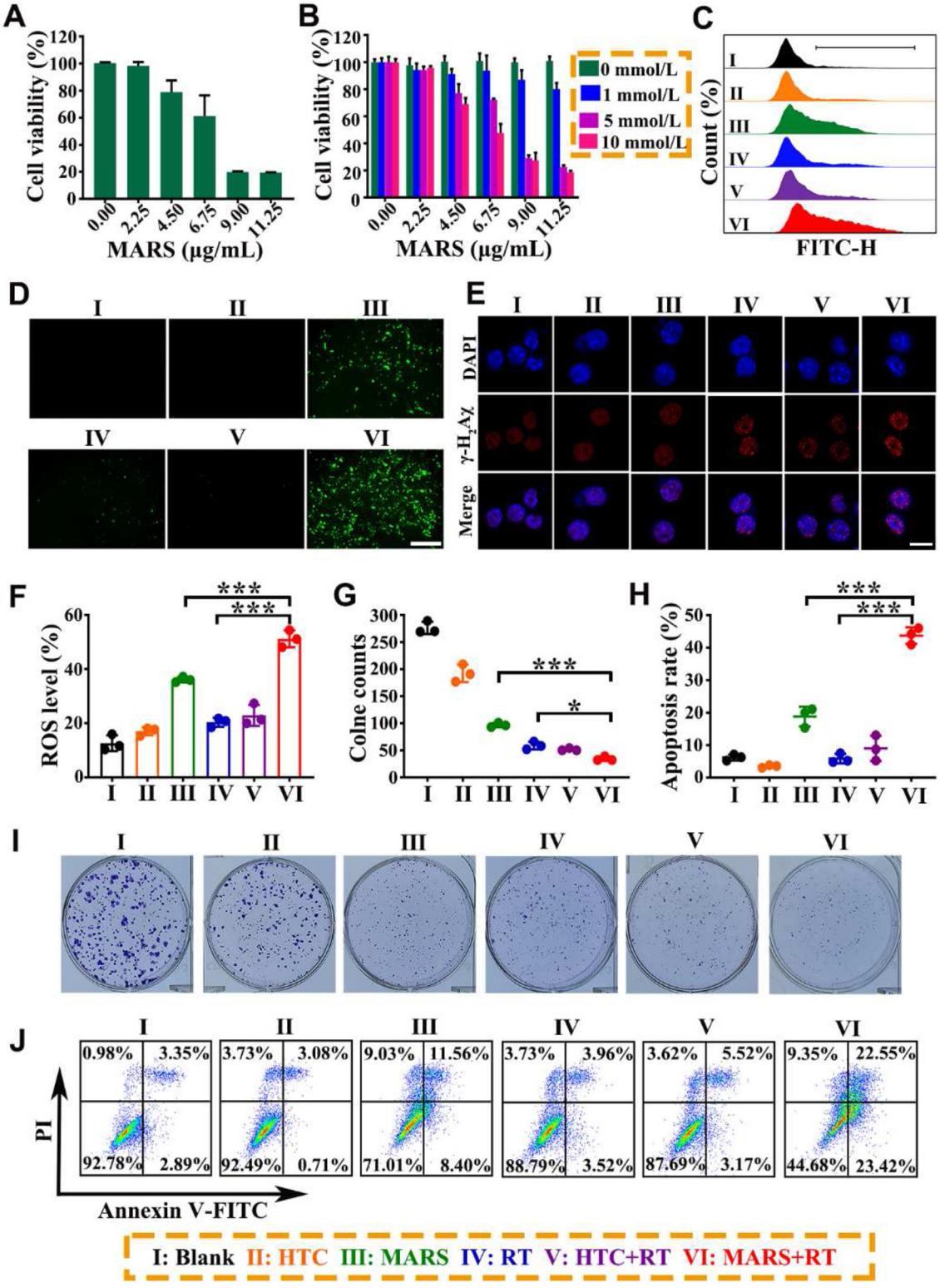

Figure 4 *In vitro* antitumor efficacy of synergistic therapy. Relative viabilities of 4T1 cells after incubation with MARS at various concentrations in the standard RPMI medium (A) or in RPMI medium containing different glucose concentrations (B). Representative fluorescence images (C) and flow cytometry (D, F) of ROS. Scale bar = 200 μm. (E) Representative CLSM images of DNA damage (γ-$H_2A\chi$: red, DAPI: blue) at 1 h after RT (4 Gy). Scale bar = 10 μm. (G, I) Representative images and quantification of 4T1 clones treated with HTC, MARS, RT (4 Gy), HTC+RT (4 Gy), or MARS+RT (4 Gy). (H, J) Representative flow cytometry plots and quantification of 4T1 cells after various treatments for 24 h. Data are presented as mean ± SD ($n = 3$). *$P < 0.05$, ***$P < 0.001$.

on the statistical results of the number of cell clones following different doses of radiotherapy (0, 2, 4, or 6 Gy) for untreated 4T1 cells (Supporting Information Fig. S9).

Next, the intracellular ROS level and DNA damage were systematically analyzed on 4T1 cells treated with PBS, HTC, and MARS without or with X-ray irradiation. Using H_2DCFDA as a fluorescence indicator, the intracellular ROS generation induced by MARS was visualized. As shown in Fig. 4D, only the MARS group exhibited weak green fluorescence in the absence of radiation. Moreover, the 4T1 cells treated with MARS+RT exhibited substantially stronger green fluorescence than RT or MARS alone, which would be attributed to the improved ROS generation combined with the Cu^+-mediated Fenton-like reactions and RT. Similarly, the flow cytometry results demonstrated a similar trend (Fig. 4C and F). In addition, the synergistic therapy of MARS and RT induced the highest foci density of γ-$H_2A\chi$ (the marker of double-stranded DNA damage) in the nuclei of all groups, indicating that MARS realized H_2O_2 self-supplying for mediating CDT and RT sensitization to facilitate oxidative stress (Fig. 4E). Next, the 4T1 tumor cell clonogenic assay was performed to evaluate the anti-proliferation effect of MARS with RT over an extended period. As illustrated in Fig. 4G and I, compared to MARS alone or X-ray irradiation alone, tumor cell clones were significantly reduced in the MARS+RT group, indicating that MARS+RT inhibited the proliferation of tumor cells effectively. Furthermore, Annexin V-FITC/PI apoptosis assays were applied to evaluate the apoptosis-inducing ability of the MARS+RT. As shown in Fig. 4H and J, upon 4 Gy of irradiation, MARS treatment elicited about 43.7 ± 2.6% of the total apoptotic ratio, whereas MARS treatment alone induced only 18.8 ± 3.0%. Meanwhile, the total apoptosis rates in HTC, RT, and HTC+RT groups were below 10.0%. These results indicated that MARS could catalyze glucose oxidation to generate abundant H_2O_2, which not only blocked the nutrition supply for cell proliferation resulting in starvation therapy, but also synergistically enhanced CDT and RT. Subsequently, the generated H_2O_2 was converted into highly toxic ROS to form radical storms *via* the Cu^+-mediated Fenton-like reaction and RT, resulting in amplified intracellular oxidative stress and inducing tumor cell damage.

3.4. ICD induction

It was known that ICD was a distinct form of cell death characterized by the release of DAMPs from dying cells. Among the DAMPs, CRT could be translocated and exposed to the tumor cell surface under the endoplasmic reticulum stress and bind with the CD91 receptor as an "eat-me" signal to aid APCs in recognizing TAAs[39]. Compared to RT or MARS alone, 4T1 tumor cells treated with MARS plus irradiation exhibited significantly brighter green fluorescence by the confocal microscopy and a rightward shift of CRT fluorescence peak by flow cytometry (Fig. 5A, B, and E). MARS+RT drastically improved the cell-surface exposure of CRT in comparison to other groups. The release of HMGB1 from the nucleus interacted with TLR-4 to stimulate proinflammatory cytokines production and DCs maturation[40,41]. As depicted in Fig. 5C, the PBS and HTC groups exhibited distinct green fluorescence in the cell nucleus, whereas the MARS+RT group only observed faint green fluorescence. Flow cytometric analyses revealed that MARS+RT treatment relocated the HMGB1 fluorescence peak of cells to the left (Fig. 5D and F). These phenomena indicated that MARS+RT could release a greater quantity of HMGB1 into the extracellular space than other groups. In addition, the secreted ATP by dying cells could bind to the P_2X_7 receptor to act as a "find-me" signal for recruiting phagocytes (*e.g.*, DCs, macrophages, monocytes, neutrophils, etc.)[42]. We evaluated ATP secretion using a luciferase-based ATP assay kit and bioluminescence methodologies. The amount of extracellular ATP treated with MARS+RT was 18.2 ± 1.2 nmol/L, which was about 1.3- or 4.5-fold more remarkable than that of MARS or RT alone, respectively (Fig. 5G). These results demonstrated that MARS efficiently facilitated RT-induced ICD effectively.

The ICD-released TAAs and DAMPs might initiate the maturation of DCs, thereby triggering immune responses. In addition, R848 binding to TLR7/8 could release multiple immunomodulatory mediators and initiate a cascade of signaling pathways, all of which promoted antigen processing and presenting ability of APCs. To verify the effects of the synergistic treatment of RT and MARS on the DCs maturation, we acquired BMDCs from C57BL/6 mice and cultured them with GM-CSF and IL-4. After that, 4T1 cells undergoing various treatments were co-incubated with BMDCs for another 24 h. The expressions of co-stimulatory molecules CD80 and CD86 were then analyzed as the typical markers of DC maturation by flow cytometry[43,44]. As shown in Fig. 5H and I, and Supporting Information Fig. S10, the expression of CD80 and CD86 in BMDCs was unaffected by HTC, RT, or HTC+RT. Significantly, MARS+RT significantly increased the proportion of mature DCs (CD80: 39.8 ± 1.1%, CD86: 29.8 ± 0.7%), in comparison with MARS (CD80: 32.9 ± 4.2%, CD86: 23.3 ± 3.5%) and RT (CD80: 26.7 ± 0.4%, CD86: 17.9 ± 0.8%). Moreover, DCs maturation ($CD11c^+CD80^+CD86^+$) was up to 57.5 ± 1.2% in the MARS+RT group, the highest of all groups (Supporting Information Fig. S11). These results suggested that amplifying RT-triggered ICD could induce potent maturation DCs to initiate systemic immunity against local or metastatic tumors (Fig. 5J).

3.5. The synergistic antitumor efficacy of RT and MARS in vivo

Following the encouraging *in vitro* results, we subsequently evaluated the antitumor efficacy of MARS with irradiation in 4T1 tumor-bearing BALB/c mice. As depicted in Fig. 6A, when the tumor sizes approached 80−100 mm^3, the tumor-bearing mice were separated at random into six groups, including saline, HTC, MARS, RT, HTC+RT, and MARS+RT groups, and they were intravenously injected every 2 days for 4 times. X-ray irradiation was performed after the second intravenous injection of saline, HTC, or MARS. In the saline group, the mice were sacrificed when tumor volumes of mice reached 1773.8 ± 145.9 mm^3. The significant inhibition effect of MARS plus irradiation could be directly observed in tumor images (Fig. 6B). As could be observed by the tumor growth curves in Fig. 6C and D, the tumor volumes of mice failed to successfully prevent tumor growth following HTC, RT, or HTC+RT treatment. In mice given MARS treatment, the average tumor volume was approximately 638.5 ± 48.8 mm^3, and tumor growth was inhibited by ~70.1%. In the MARS+RT group, the average tumor volume was about 342.1 ± 67.3 mm^3, and it exhibited a more substantial tumor suppression effect with ~83.2% inhibition of tumor growth than that of the MARS group ($P < 0.01$), attributable to the cascade amplified systemic antitumor immunity of the synergistic treatment of MARS and RT. The same trend of tumor suppression was observed in the tumor weights analysis (Fig. 6E). To evaluate further the antitumor efficacy of MARS and RT, tumor growth was measured in mice treated with HSA+R848+TA (HRT), HSA+GOx+Cu^{2+}+TA

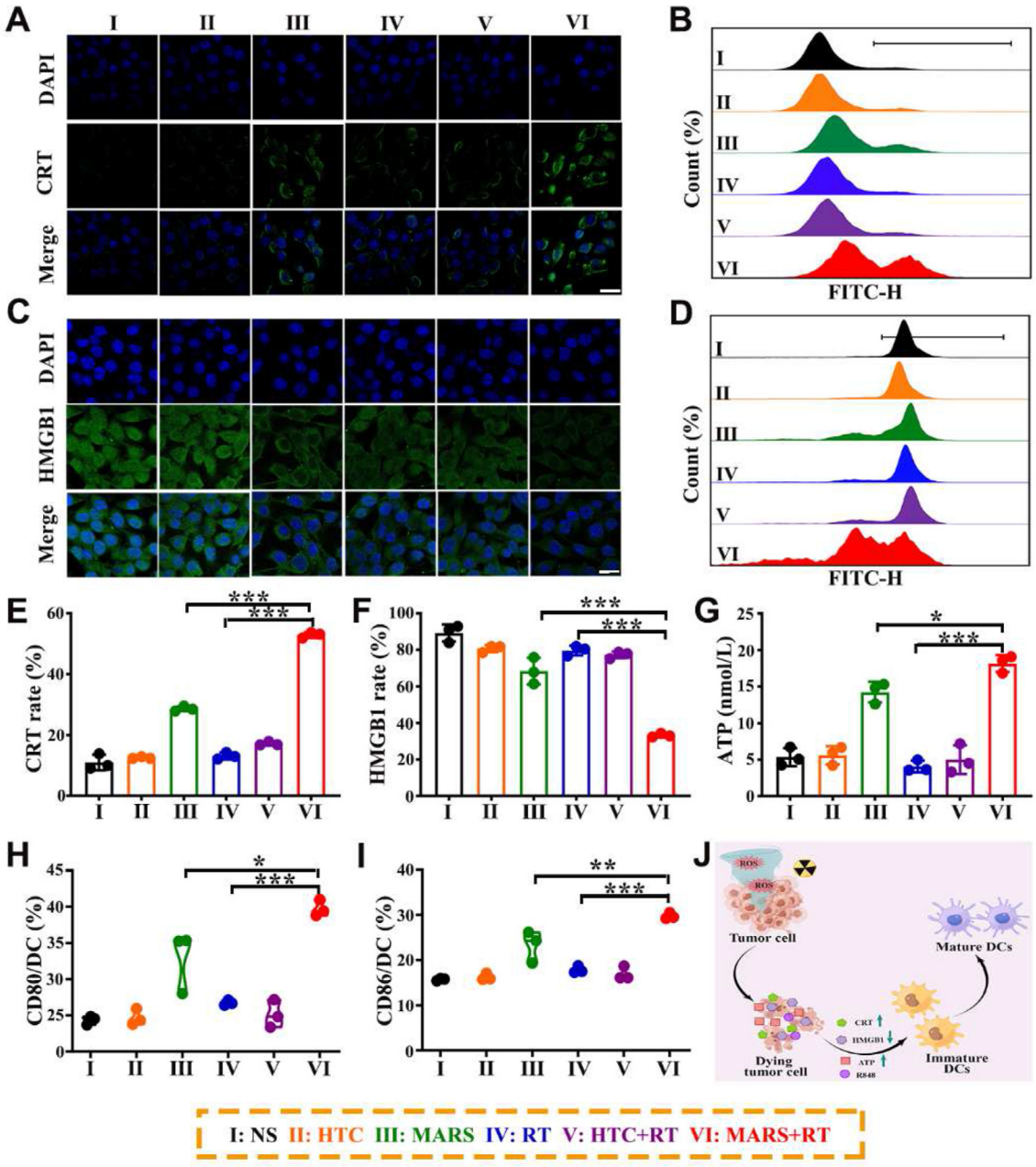

Figure 5 Immunogenic cell death inducted DCs maturation. CRT expression analysis on 4T1 cells after various treatments by CLSM (A) and flow cytometry (B, E). Scale bars = 20 μm. Representative CLSM images (C) and flow cytometry (D, F) of HMGB1 on 4T1 cells treated with different treatments. Scale bars = 20 μm. (G) Release of ATP by 4T1 cells after various treatments for 24 h. The expressions of CD80 (H) and CD86 (I) on BMDCs by flow cytometry. (J) The mechanism illustration of ICD-inducing DCs maturation. Data are presented as mean ± SD ($n = 3$). *$P < 0.05$, **$P < 0.01$, ***$P < 0.001$.

(HGTC), HRT+RT and HGTC+RT, and the treatment schedule was shown in Supporting Information Fig. S12A. As shown in Supporting Information Fig. S12B, S13A and S13B, compared to the rapid growth of controls, the MARS+RT group exhibited the maximum tumor suppression with the smallest average tumor volume (169.9 ± 23.3 mm^3, $P < 0.001$), which was significantly superior to HRT (702.2 ± 58.9 mm^3, $P < 0.001$), HGTC (404.1 ± 41.1 mm^3, $P < 0.001$), HRT+RT (539.0 ± 38.0 mm^3, $P < 0.001$) and HGTC+RT (374.8 ± 7.6 mm^3, $P < 0.001$). The tumor weight provided additional evidence to support the remarkable antitumor effect of MARS+RT (Supporting Information Fig. S13C). Additionally, the mice treated with MARS lived about 37 days, whereas mice in the MARS+RT group had a significantly longer lifespan of 49 days ($P < 0.1$, Fig. 6F).

Furthermore, there was negligible variation in the body weight of mice among all treated groups, indicating that these treatments had no discernible effect on the health of mice (Fig. 6G and Supporting Information Fig. S13D). H&E staining of major organs in the MARS+RT group revealed no substantial damage compared to the other group, further confirming the safety of the MARS+RT (Supporting Information Fig. S14). Afterward, tumor

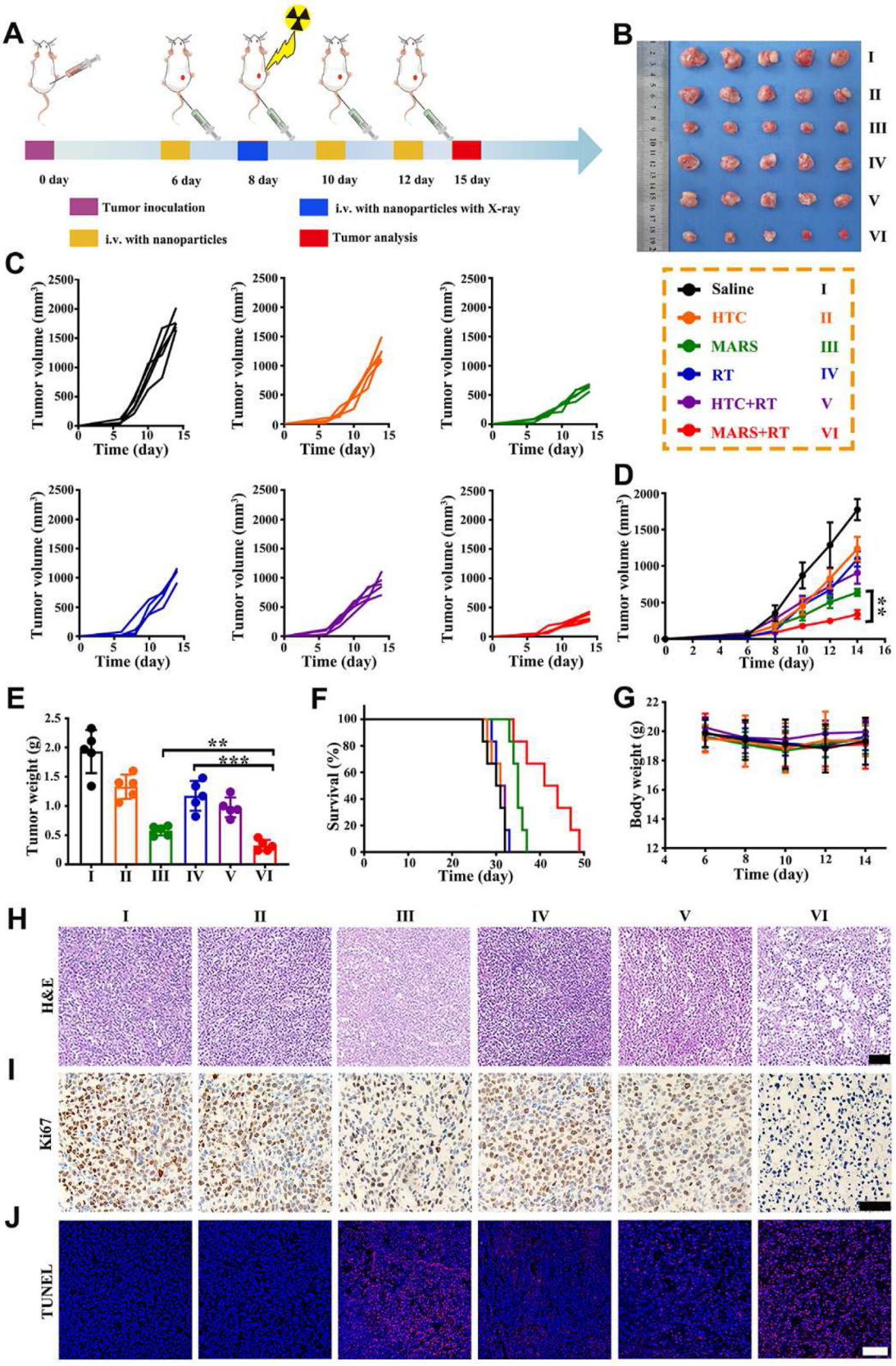

Figure 6 Antitumor effect of MARS+RT against 4T1 subcutaneous xenograft model. (A) Treatment schedule of MARS combined with RT. (B) Photographs of tumors from the mice after various treatments on Day 15. (C) Individual tumor growth curve in each group. (D) Average tumor volume curves, (E) tumor weight, (F) survival rate, and (G) body weight of mice with different treatments. (H) H&E, (I) Ki67, and (J) TUNEL stained tumor sections of different groups. Scale bars = 100 μm. Data are presented as mean ± SD ($n = 5$). $^{**}P < 0.01$, $^{***}P < 0.001$.

tissues were stained with H&E, Ki67, and TUNEL to evaluate cell damage induced by various treatments. As shown in Fig. 6H, the tumors flourished with densely arranged cells and normal nuclei in the NS group. However, the tumor tissue morphology of mice treated with MARS+RT was markedly different from that of the other groups, with extensive nuclear shrinkage and disorganized cell arrangement attributable to the synergistic effect of MARS and RT on the inhibition of proliferation. The Ki67 assay further confirmed that the MARS+RT group demonstrated the lowest cell proliferation among all the groups (Fig. 6I). The TUNEL results exhibited that the MARS+RT group's tumor tissues had the largest apoptosis region compared to those in the other treatments groups (Fig. 6J). All the above research results confirmed that the MARS combined with X-ray irradiation exhibited robust antitumor activity.

3.6. *Regulation of tumor microenvironment*

Since MARS+RT exhibited excellent tumor suppression, we further investigated the potential mechanism of MARS+RT synergistic antitumor efficacy in greater detail. Therefore, the various groups' tumors, TDLNs, and spleens were collected and evaluated for immune response activation using flow cytometry. As exhibited in Fig. 7A and B, the percentage of $CD11c^{+}CD80^{+}CD86^{+}$ in TDLNs was substantially more remarkable in the MARS+RT group (20.3 ± 0.5%) compared with the other groups (NS:

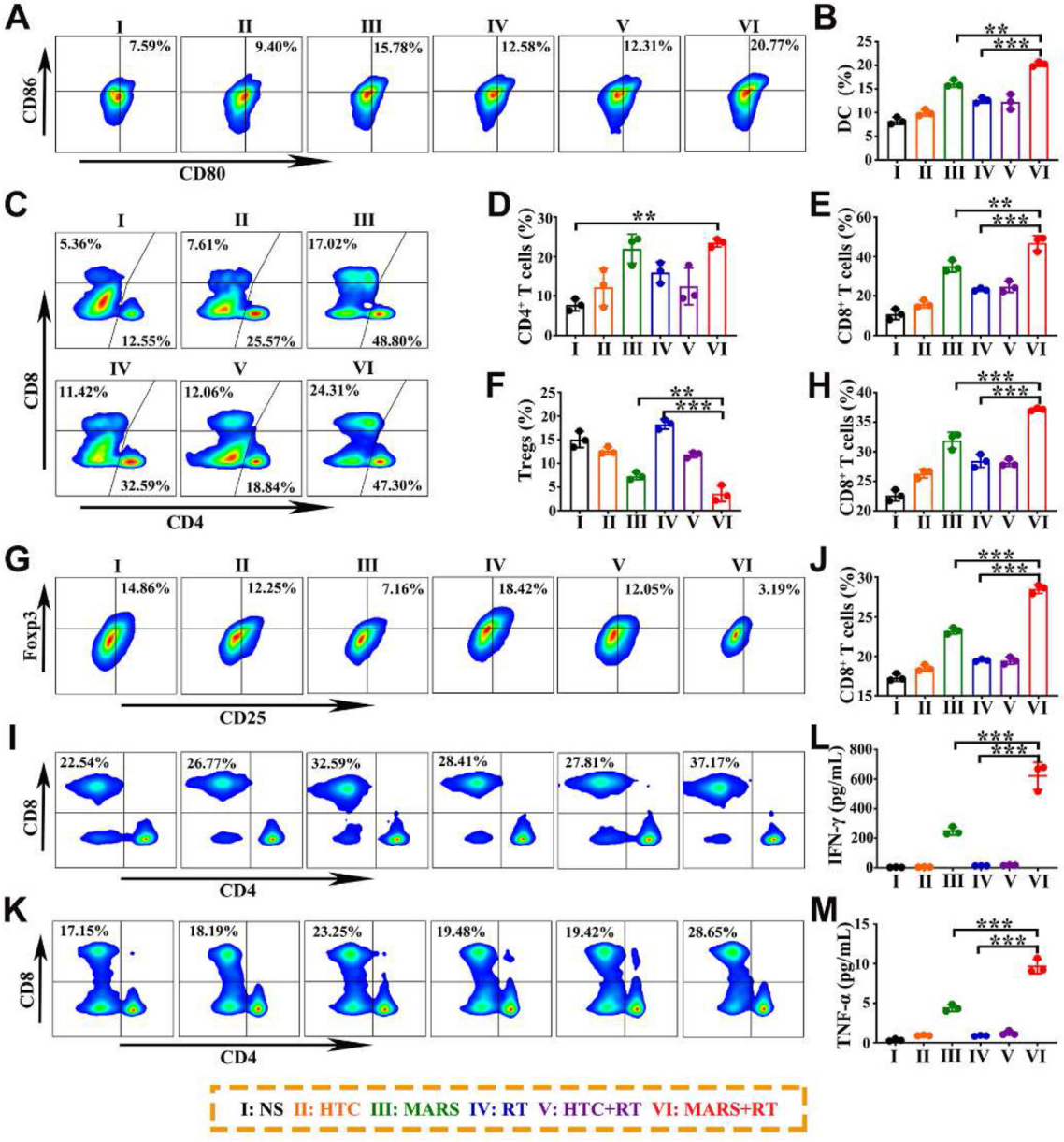

Figure 7 Potent antitumor immune response initiated by MARS combined with RT. Representative flow cytometry plots (A) and (B) quantification of DCs maturation in TDLNs. Flow cytometric plots (C) of $CD4^{+}$ and $CD8^{+}$ cells in tumors after treatments and corresponding quantification results (D, E). (F, G) The expression of Tregs in tumors and quantitative analysis. The flow cytometric analysis of $CD8^{+}$ T cells in TDLNs (H, I) and spleens (J, K) from various groups. The expression levels of TNF-γ (L) and IFN-α (M) in the serum. Data are presented as mean ± SD ($n = 3$). $^{**}P < 0.01$, $^{***}P < 0.001$.

8.3 ± 0.8%, HTC: 10.0 ± 0.7%, MARS: 16.1 ± 0.8%, RT: 12.6 ± 1.6%, HTC+RT: 12.3 ± 0.5%). These results indicated that MARS+RT-induced ICD could stimulate DCs maturation, thereby improving antitumor immunity. Because the functions of DCs, such as antigen recognition and cross-presentation, were typically impaired in tumor microenvironments, we investigated the activation of T lymphocytes at the tumor site. The percentages of helper T lymphocytes ($CD3^+CD4^+$) and cytotoxic T lymphocytes (CTLs, $CD3^+CD8^+$) in the tumor were much higher in the MARS+RT group (46.9 ± 2.1% and 23.4 ± 1.9%) than that in the MARS (43.9 ± 7.4% and 17.5 ± 1.5%) or RT (31.9 ± 5.3% and 11.6 ± 0.4%) group, further confirmed the crucial role of MARS for cascade-amplified RT-mediated the infiltration of T cell (Fig. 7C–E and Supporting Information Fig. S15). Since Tregs could inhibit the antitumor immune response of CTLs, we investigated the levels of immunosuppressive Tregs ($CD4^+CD25^+FoxP3^+$) following various treatments. The combination with RT, the MARS significantly decreased the proportion of Tregs (3.6 ± 1.7%) in comparison with other groups such as NS (15.0 ± 1.7%), HTC (12.6 ± 0.8%), MARS (7.3 ± 0.8%, $P < 0.01$), RT (18.3 ± 1.0%, $P < 0.001$), and HTC+RT (11.8 ± 0.6%) (Fig. 7F and G).

In addition, we evaluated whether the MARS+RT could induce systemic antitumor immune responses. After various therapies, the activated $CD3^+CD8^+$ T effector cells in the TDLNs were analyzed. The ratio of $CD3^+CD8^+$ in the TDLNs was significantly higher in the MARS+RT group (37.2 ± 0.3%) than in the MARS (31.9 ± 1.4%, $P < 0.001$) or RT (28.5 ± 1.1%, $P < 0.001$) group (Fig. 7H and I, and Supporting Information Fig. S16). Intriguingly, A similar trend of $CD3^+CD8^+$ was observed in the spleens after treatment with MARS and RT (Fig. 7J and K, and Supporting Information Fig. S17). These results indicated that MARS+RT successfully initiated system antitumor immunity. Besides, based on the above positive regulation, we further determined the concentration of IFN-γ and TNF-α in the serum of mice receiving various formulations. As anticipated, the concentrations of IFN-γ and TNF-α were highest after being treated with MARS+RT, which were 2.5- and 2.2-fold higher than the MARS group, respectively (Fig. 7L and M). Collectively, these results indicated that the synergistic therapy of

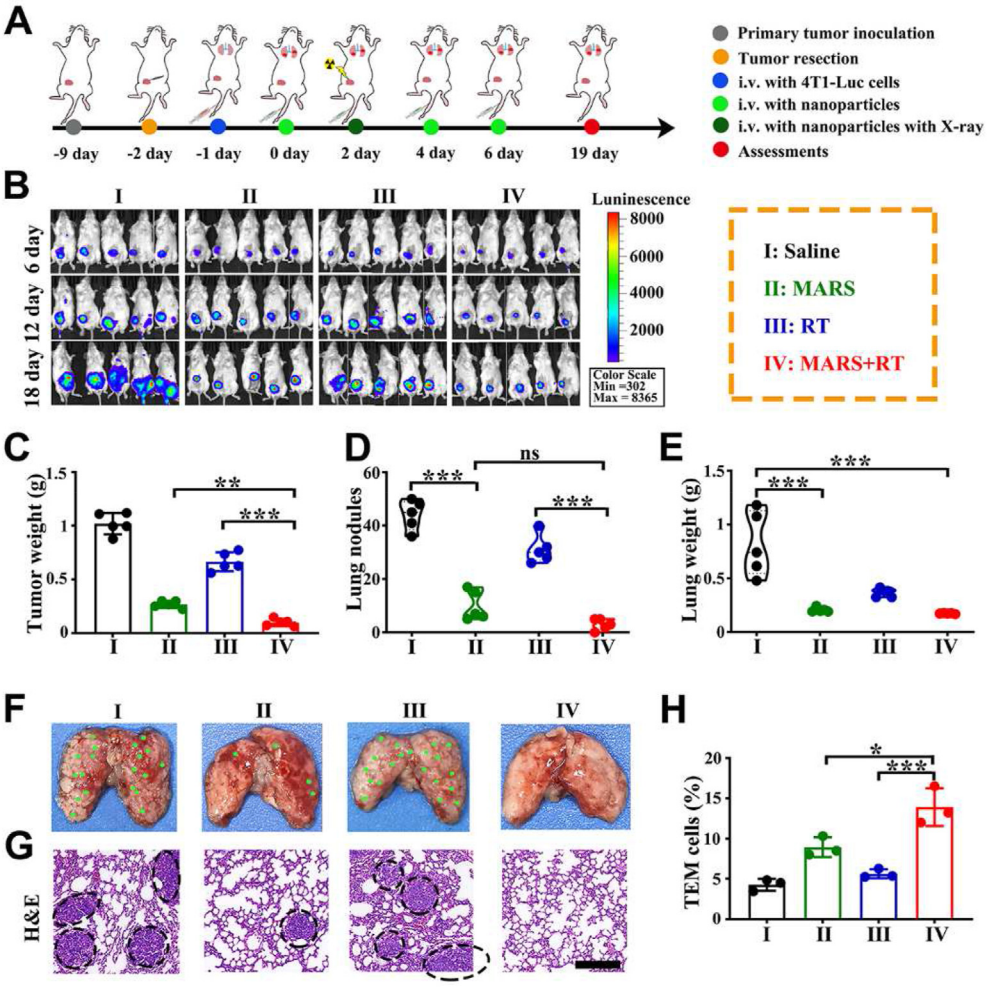

Figure 8 Therapeutic activity of MARS+RT in the 4T1 tumor postoperative recurrence and pulmonary metastasis model. (A) Treatment schedule of MARS combined with RT. (B) *In vivo* bioluminescence imaging of mice after being treated with NS, MARS, RT, and MARS+RT on Days 6, 12, and 18 ($n = 5$). (C) Recurrent tumor weight, (D) metastatic lung nodules, and (E) lung weights after various treatments ($n = 5$). (F) Representative pictures and (G) H&E staining of lungs in each group. Scale bar = 100 μm. (H) Percentages of TEMs in spleens analyzed by flow cytometry ($n = 3$). Data are presented as mean ± SD. *$P < 0.05$, **$P < 0.01$, ***$P < 0.001$. *n*s, not significant.

RT and MARS could induce cascade-amplification of systemic immunologic responses to achieve a more potent antitumor effect.

3.7. *Effective inhibition of postoperative recurrence and pulmonary metastasis by MARS+RT*

Typically, postoperative recurrence was triggered by the proliferation and migration of residual tumor cells, which increased the mortality rate[45,46]. Based on the schematic diagram described in Fig. 8A, we subsequently assessed the excellent antitumor efficacy of MARS+RT on the 4T1 tumor postoperative recurrence model. The orthotopic TNBC tumor model was established using 4T1-Luc cells. Furthermore, to simulate the presence of residual tumor cells that might be present during surgery, about 10% of each mouse's original tumor was retained when the tumor volume reached about 200 mm^3. Then, we utilized bioluminescence imaging to monitor the recurrence of tumors following surgery and treatment with various formulations. As shown in Fig. 8B, the fluorescence intensity of the NS group exhibited varying degrees of tumor recurrence within the first 8 days, whereas the fluorescence intensity of the NS, MARS, and RT groups increased gradually in a time-dependent manner up to 18 days. Intriguingly, MARS+RT treatment maintained a low level of tumor fluorescence, indicating that MARS+RT effectively prevented postoperative tumor recurrence. Moreover, the tumor weight was consistent with the results of bioluminescence images, with the highest tumor inhibition rate (∼90.3%) in the MARS+RT group among all groups (RT: ∼29.1%, $P < 0.001$, MARS: ∼77.3%, $P < 0.001$) (Fig. 8C and Supporting Information Fig. S18). In the 4T1 pulmonary metastasis model, we further confirmed the therapeutic efficacy of MARS+RT. Treatment with MARS+RT restrained pulmonary metastasis most efficiently, and the MARS+RT exhibited a significant suppression ratio (∼93.2%) compared to the RT group (Fig. 8D−F). In addition, H&E lung staining of the MARS+RT group revealed the lowest number of lung tumor nodules (Fig. 8G). Using flow cytometry, we quantified the percentage of memory T cells in the spleen to determine whether the immunologic memory effect induced by MARS+RT suppressed postoperative recurrence and pulmonary metastasis. As depicted in Fig. 8H and Supporting Information Fig. S19, the percentage of effector memory T (TEM, $CD3^+CD8^+CD44^+CD62L^-$) cells in the MARS+RT group (13.9 ± 2.3%) was higher than that of the MARS (8.9 ± 1.2%, $P < 0.05$) or X-ray radiation (5.6 ± 0.6%, $P < 0.001$) alone. These results confirmed that the synergistic therapy of MARS and RT could initiate cascade-amplified antitumor immune responses that effectively inhibited postoperative recurrence and pulmonary metastasis.

4. Conclusions

In summary, we fabricated multifunctional self-sufficient nanoparticles to trigger radical storms and activate the cascade-amplified systemic immune responses against local tumors, postoperative recurrence, and metastasis. The MARS was constructed with dual-enzyme activity (GOx and peroxidase-like) and R848 agonist *via* an HSA-mediated biomineralization-like method. Upon administration intravenously, the MARS aggregated at the tumor site and disintegrated rapidly in the acidic microenvironment, releasing GOx, Cu^{2+}, TA, and R848. The released GOx could catalyze the consumption of glucose to generate H_2O_2 and lactic acid, which not only limited the Warburg effect of tumor cells to achieve starvation therapy and diminished the inhibitory effect of Tregs, but also achieved H_2O_2 self-supplying to generate •OH *via* Cu^+-mediated Fenton-like reaction. Meanwhile, ionizing radiation could convert generated H_2O_2 into ROS to enhance RT-mediated tumoricidal effects. Then, the ROS generated by RT and CDT could form radical storms that induced a robust ICD effect for initiating systemic immune responses. When MARS was combined with RT to treat 4T1 tumors *in vivo*, the tumor suppression rate reached ∼83.2%, and the survival time of mice was substantially extended to 49 days. MARS+RT promoted the activation of DCs, amplified $CD8^+$ T cell response, and alleviated the immunosuppressive tumor microenvironment to initiate the cascade-amplified systemic immune responses, resulting in an excellent therapeutic effect. Furthermore, MARS+RT could be used as adjuvant therapy to inhibit postoperative recurrence and exhibited a suppression ratio of ∼93.2% in pulmonary metastasis. Therefore, we provided an innovative strategy to trigger radical storms to elicit a robust ICD effect and activate cascade-amplified systemic immunity for cancer treatment.

Acknowledgments

This work was financially supported by the National Natural Science Foundation of China (82172094) and Funds of Sichuan Province for Distinguished Young Scholar (2021JDJQ0037, China). Fig. 5J was drawn by Figdraw (www.figdraw.com).

Author contributions

Changyang Gong, Liping Bai and Qinjie Wu designed the research. Liping Bai and Jin Yang carried out the experiments, performed data analysis, and wrote the manuscript. Siting Yu, Zhongzheng Xiang, and Yuanyuan Zeng assisted experiments. Meiling Shen and Xiaorong Kou participated in part of the experiments. All of the authors have read and approved the final manuscript.

Conflicts of interest

The authors declare no conflicts of interest.

Appendix A. Supporting information

Supporting data to this article can be found online at https://doi.org/10.1016/j.apsb.2023.10.003.

References

1. Atun R, Jaffray DA, Barton MB, Bray F, Baumann M, Vikram B, et al. Expanding global access to radiotherapy. *Lancet Oncol* 2015;**16**:1153−86.
2. Chinnaiyan AM, Prasad U, Shankar S, Hamstra DA, Shanaiah M, Chenevert TL, et al. Combined effect of tumor necrosis factor-related apoptosis-inducing ligand and ionizing radiation in breast cancer therapy. *Proc Natl Acad Sci U S A* 2000;**97**:1754−9.
3. Song GS, Cheng L, Chao Y, Yang K, Liu Z. Emerging nanotechnology and advanced materials for cancer radiation therapy. *Adv Mater* 2017;**29**:1700996.
4. Garg AD, Nowis D, Golab J, Vandenabeele P, Krysko DV, Agostinis P. Immunogenic cell death, DAMPs and anticancer therapeutics: an emerging amalgamation. *Biochim Biophys Acta* 2010;**1805**:53−71.

5. Li ZL, Lai XQ, Fu SQ, Ren L, Cai H, Zhang H, et al. Immunogenic cell death activates the tumor immune microenvironment to boost the immunotherapy efficiency. *Adv Sci* 2022;**9**:e2201734.
6. Kroemer G, Galluzzi L, Kepp O, Zitvogel L. Immunogenic cell death in cancer therapy. *Annu Rev Immunol* 2013;**31**:51−72.
7. Rodríguez-Ruiz ME, Vanpouille-Box C, Melero I, Formenti SC, Demaria S. Immunological mechanisms responsible for radiation-induced abscopal effect. *Trends Immunol* 2018;**39**:644−55.
8. Yu XJ, Ma HT, Xu GY, Liu Z. Radiotherapy assisted with biomaterials to trigger antitumor immunity. *Chin Chem Lett* 2022;**33**:4169−74.
9. Deutsch E, Chargari C, Galluzzi L, Kroemer G. Optimising efficacy and reducing toxicity of anticancer radioimmunotherapy. *Lancet Oncol* 2019;**20**:e452−63.
10. McLaughlin M, Patin EC, Pedersen M, Wilkins A, Dillon MT, Melcher AA, et al. Inflammatory microenvironment remodelling by tumour cells after radiotherapy. *Nat Rev Cancer* 2020;**20**:203−17.
11. Zhang WC, Yan CH, Gao X, Li XX, Cao FL, Zhao G, et al. Safety and feasibility of radiotherapy plus camrelizumab for locally advanced esophageal squamous cell carcinoma. *Oncol* 2021;**26**:e1110−24.
12. Xu YY, Xiong JY, Sun XY, Gao HL. Targeted nanomedicines remodeling immunosuppressive tumor microenvironment for enhanced cancer immunotherapy. *Acta Pharm Sin B* 2022;**12**:4327−47.
13. Gao J, Wang WQ, Pei Q, Lord MS, Yu HJ. Engineering nanomedicines through boosting immunogenic cell death for improved cancer immunotherapy. *Acta Pharmacol Sin* 2020;**41**:986−94.
14. Duan XP, Chan C, Lin WB. Nanoparticle-mediated immunogenic cell death enables and potentiates cancer immunotherapy. *Angew Chem Int Ed Engl* 2019;**58**:670−80.
15. Zhu L, Luo MY, Zhang YF, Fang F, Li M, An FF, et al. Free radical as a double-edged sword in disease: deriving strategic opportunities for nanotherapeutics. *Coord Chem Rev* 2023;**475**:214875.
16. Li JY, Zhang YQ, Yu MR, Wang AH, Qiu Y, Fan WW, et al. The upregulated intestinal folate transporters direct the uptake of ligand-modified nanoparticles for enhanced oral insulin delivery. *Acta Pharm Sin B* 2022;**12**:1460−72.
17. Tang ZM, Zhao PR, Wang H, Liu YY, Bu WB. Biomedicine meets Fenton chemistry. *Chem Rev* 2021;**121**:1981−2019.
18. Guo YX, Jia HR, Zhang XD, Zhang XP, Sun Q, Wang SZ, et al. A glucose/oxygen-exhausting nanoreactor for starvation-and hypoxia-activated sustainable and cascade chemo-chemodynamic therapy. *Small* 2020;**16**:e2000897.
19. Fu LH, Wan YL, Qi C, He J, Li CY, Yang C, et al. Nanocatalytic theranostics with glutathione depletion and enhanced reactive oxygen species generation for efficient cancer therapy. *Adv Mater* 2021;**33**:e2006892.
20. Li XC, Luo R, Liang XQ, Wu QJ, Gong CY. Recent advances in enhancing reactive oxygen species based chemodynamic therapy. *Chin Chem Lett* 2022;**33**:2213−30.
21. Fu LH, Qi C, Hu YR, Lin J, Huang P. Glucose oxidase-instructed multimodal synergistic cancer therapy. *Adv Mater* 2020;**32**:e2003130.
22. Hao Y, Dong ZL, Chen MC, Chao Y, Liu Z, Feng LZ, et al. Near-infrared light and glucose dual-responsive cascading hydroxyl radical generation for in situ gelation and effective breast cancer treatment. *Biomaterials* 2020;**228**:119568.
23. De Rosa V, Di Rella F, Di Giacomo A, Matarese G. Regulatory T cells as suppressors of anti-tumor immunity: role of metabolism. *Cytokine Growth Factor Rev* 2017;**35**:15−25.
24. Medzhitov R. Toll-like receptors and innate immunity. *Nat Rev Immunol* 2001;**1**:135−45.
25. Bahmani B, Gong H, Luk BT, Haushalter KJ, DeTeresa E, Previti M, et al. Intratumoral immunotherapy using platelet-cloaked nanoparticles enhances antitumor immunity in solid tumors. *Nat Commun* 2021;**12**:1999.
26. Chen Q, Chen JW, Yang ZJ, Xu J, Xu LG, Liang C, et al. Nanoparticle-enhanced radiotherapy to trigger robust cancer immunotherapy. *Adv Mater* 2019;**31**:e1802228.
27. Chi HJ, Li CM, Zhao FS, Zhang L, Ng TB, Jin GY, et al. Anti-tumor activity of toll-like receptor 7 agonists. *Front Pharmacol* 2017;**8**:304.
28. Alam MM, Yang D, Trivett A, Meyer TJ, Oppenheim JJ. HMGN1 and R848 synergistically activate dendritic cells using multiple signaling pathways. *Front Immunol* 2018;**9**:2982.
29. Michaelis KA, Norgard MA, Zhu X, Levasseur PR, Sivagnanam S, Liudahl SM, et al. The TLR7/8 agonist R848 remodels tumor and host responses to promote survival in pancreatic cancer. *Nat Commun* 2019;**10**:4682.
30. Ye J, Mills BN, Qin SS, Garrett-Larsen J, Murphy JD, Uccello TP, et al. Toll-like receptor 7/8 agonist R848 alters the immune tumor microenvironment and enhances SBRT-induced antitumor efficacy in murine models of pancreatic cancer. *J Immunother Cancer* 2022;**10**:e004784.
31. Song QX, Lan GD, Li Q, Lin Y, Chen X, Liu H, et al. A hydrogel-enabled cascade amplification of radiosensitization and immune activation for cancer radiotherapy. *Chem Eng J* 2023;**462**:142201.
32. Zhu XQ, Wang XX, Li BY, Zhang Y, Chen YL, Zhang WY, et al. A three-in-one assembled nanoparticle containing peptide-radiosensitizer conjugate and TLR7/8 agonist can initiate the cancer-immunity cycle to trigger antitumor immune response. *Small* 2022;**18**:e2107001.
33. Liu ZB, Chen XY. Simple bioconjugate chemistry serves great clinical advances: albumin as a versatile platform for diagnosis and precision therapy. *Chem Soc Rev* 2016;**45**:1432−56.
34. Chen Q, Feng LZ, Liu JJ, Zhu WW, Dong ZL, Wu YF, et al. Intelligent albumin-MnO_2 nanoparticles as pH-/H_2O_2-responsive dissociable nanocarriers to modulate tumor hypoxia for effective combination therapy. *Adv Mater* 2016;**28**:7129−36.
35. Chen Q, Liu Z. Albumin carriers for cancer theranostics: a conventional platform with new promise. *Adv Mater* 2016;**28**:10557−66.
36. Ogawa Y. Paradigm shift in radiation biology/radiation oncology-exploitation of the "H_2O_2 effect" for radiotherapy using low-LET (linear energy transfer) radiation such as X-rays and high-energy electrons. *Cancers* 2016;**8**:28.
37. Liu PY, Miao ZH, Li K, Yang HJ, Zhen L, Xu CY. Biocompatible Fe^{3+}-TA coordination complex with high photothermal conversion efficiency for ablation of cancer cells. *Colloids Surf B Biointerfaces* 2018;**167**:183−90.
38. An L, Yan CL, Mu XL, Tao C, Tian QW, Lin JM, et al. Paclitaxel-induced ultrasmall gallic acid-Fe@BSA self-assembly with enhanced MRI performance and tumor accumulation for cancer theranostics. *ACS Appl Mater Interfaces* 2018;**10**:28483−93.
39. Obeid M, Tesniere A, Ghiringhelli F, Fimia GM, Apetoh L, Perfettini J, et al. Calreticulin exposure dictates the immunogenicity of cancer cell death. *Nat Med* 2007;**13**:54−61.
40. Apetoh L, Ghiringhelli F, Tesniere A, Criollo A, Ortiz C, Lidereau R, et al. The interaction between HMGB1 and TLR4 dictates the outcome of anticancer chemotherapy and radiotherapy. *Immunol Rev* 2007;**220**:47−59.
41. Saenz R, Futalan D, Leutenez L, Eekhout F, Fecteau JF, Sundelius S, et al. TLR4-dependent activation of dendritic cells by an HMGB1-derived peptide adjuvant. *J Transl Med* 2014;**12**:211.
42. Elliott MR, Chekeni FB, Trampont PC, Lazarowski ER, Kadl A, Walk SF, et al. Nucleotides released by apoptotic cells act as a find-me signal to promote phagocytic clearance. *Nature* 2009;**461**:282−6.
43. Dilioglou S, Cruse JM, Lewis RE. Function of CD80 and CD86 on monocyte-and stem cell-derived dendritic cells. *Exp Mol Pathol* 2003;**75**:217−27.
44. Liang XQ, Li L, Li XC, He T, Gong SL, Zhu SY, et al. A spontaneous multifunctional hydrogel vaccine amplifies the innate immune response to launch a powerful antitumor adaptive immune response. *Theranostics* 2021;**11**:6936−49.
45. Lukianova-Hleb EY, Kim Y-S, Belatsarkouski I, Gillenwater AM, O'Neill BE, Lapotko DO. Intraoperative diagnostics and elimination of residual microtumours with plasmonic nanobubbles. *Nat Nanotechnol* 2016;**11**:525−32.
46. Conde J, Oliva N, Zhang Y, Artzi N. Local triple-combination therapy results in tumour regression and prevents recurrence in a colon cancer model. *Nat Mater* 2016;**15**:1128−38.